# Large-Field CO ($J = 1{\rightarrow}0$) Observations of the Starburst Galaxy M 82

Dragan SALAK, Naomasa NAKAI, and Yusuke MIYAMOTO

*Department of Physics, Graduate School of Pure and Applied Sciences, University of Tsukuba,*
*Tennodai 1-1-1 Tsukuba, Ibaraki 305-8571*
*s1130080@u.tsukuba.ac.jp*

Aya YAMAUCHI

*Mizusawa VLBI Observatory, National Astronomical Observatory of Japan, 2-12 Hoshigaoka, Mizusawa, Oshu, Iwate 023-0861*

and

Takeshi G. TSURU

*Department of Physics, Faculty of Science, Kyoto University, Kitashirakawa-Oiwake-Cho, Sakyo, Kyoto 606-8502*

### Abstract

We present large-field ($15.7 \times 16.9$ arcmin$^2$) CO ($J = 1{\rightarrow}0$) observations of the starburst galaxy M 82, at an angular resolution of $22''$ with the NRO 45-m telescope. The CO emission was detected in the galactic disk, outflow (driven by the galactic wind) up to $\sim 2$ kpc above the galactic plane in the halo, and in tidal streams. The kinematics of the outflow (including CO line splitting) suggests that it has the shape of a cylinder that is diverging outwards. The mass and kinetic energy of the molecular gas outflow are estimated to be $(0.26–1.0) \times 10^9 \, M_\odot$ and $(1–4) \times 10^{56}$ erg. A clump of CO gas was discovered 3.5 kpc above the galactic plane; it coincides with a dark lane previously found in X-ray observations, and a peak in H I emission. A comparison with H I, hot molecular hydrogen and dust suggests that the molecular gas shows signatures of warm and cool components in the outflow and tidal streams, respectively.

**Key words:** galaxies: individual (M 82) — galaxies: interactions — galaxies: ISM — galaxies: starburst

## 1. Introduction

During the last fifty years we have witnessed increasing evidence suggesting that a considerable number of galaxies host galactic winds. Pioneering works, e.g., Lynds and Sandage (1963), reported the discovery of an "explosion" in the galaxy M 82, and various observational data lead us to conclude that the origin of such violent processes must be in the galactic nuclei where either vigorous star formation (starburst), or a supermassive black hole (in active galactic nuclei, AGN), or both act as the sources that release huge amounts of energy that drive the winds (e.g., Tenorio-Tagle & Bodenheimer 1988; Veilleux et al. 2005). Enhanced nuclear activity is often suspected to be triggered by environmental effects, such as tidal interactions when galaxies collide or pass each other at a distance close enough to disturb their morphology. This may be the case especially with galaxies, that are group members; a remarkable example is the M 81–M 82 system in which M 81 has fairly open spiral arms and a low-luminosity AGN in its center (e.g., Miller et al. 2010), while M 82 is a starburst with a galactic wind and tidal arms (e.g., Yun et al. 1994). Bursts of star formation are found in galaxies that contain large amounts of molecular gas and dust. Unlike in ordinary late-type galaxies, in starbursts many new stars are born rapidly (faster than can be sustained during the lifetime of the host galaxy), and in some cases frequent supernova (SN) explosions lead to the formation of galactic winds associated with large-scale outflows of various components of the interstellar medium (ISM) (e.g., Veilleux et al. 2005).

Although many studies have recently been devoted to understanding the properties of the power sources behind the outflows in starbursts and AGN (e.g., Murray et al. 2005; Narayanan et al. 2008; Chung et al. 2011; Aalto et al. 2012), observational data of the halo regions of such galaxies remain sparse. Without large-scale observations of the halo, it is difficult to estimate the extent of the feedback triggered by the nuclear activity. Therefore, in order to study galactic winds in detail, and to obtain a full picture of the host galaxy, the physical conditions of the gas and the energetics linked to the central engine, two approaches are equally important: observations of all components of the ISM, and on all scales. For instance, while optical and X-ray observations reveal the ionized-warm and hot gas component, observations of the extra-planar molecular gas yield information on the distribution and kinematics of the neutral material. A particularly easy way to trace the molecular gas is to observe the rotational lines of carbon monoxide (CO). CO is a very stable diatomic molecule, abundant in the ISM, with bright rotational transition lines in a broad range of densities and temperatures—good tracer of dense and diffuse molecular gas. In recent years, the efficiency of wide-field CO observations has improved significantly since the development of multi-beam receivers on single-dish telescopes; they now provide rapid mapping in short intervals of time.

M 82 is one of the nearest (3.53 Mpc, Karachentsev et al. 2002) and brightest starburst galaxies with a prominent galactic wind. The galaxy is a particularly good observational target for studying the extra-planar ISM because of the high inclination of its galactic plane ($i = 80°$, de Vaucouleurs et al. 1991). One of the first observational summaries and interpretations of the nuclear activity of M 82 was given in Rieke et al. (1980). Nakai et al. (1987) were among the first to suggest that

**Table 1.** Basic parameters of M 82.

| | |
|---|---|
| Distance* | 3.53 Mpc |
| Receding velocity† | 220 km s$^{-1}$ |
| Right ascension (J2000.0)‡ | 9$^{\rm h}$55$^{\rm m}$52$^{\rm s}$63 |
| Declination (J2000.0)‡ | 69°40′47″1 |
| Morphological type§ | S0 |
| Position angle‖ | 65° |
| Inclination angle♯ | 80° |

\* Karachentsev et al. (2002); $1' = 1.03$ kpc.
† Oloffson and Rydbeck (1984); LSR (radio).
‡ Rieke et al. (1980); corresponds to the 2.2-$\mu$m peak emission.
§ Ichikawa et al. (1995).
‖ Nielson (1973).
♯ de Vaucouleurs et al. (1991).

**Table 2.** Summary of observations.

| | |
|---|---|
| Telescope | NRO 45 m |
| Observing period | 2009 March |
| | 2010 February, April, May |
| Receiver (obs.mode) | BEARS (OTF) |
| Spectrometer (full BW) | AC (512 MHz) |
| Total integration time* | 15.2 h |
| Observed spectral line | $^{12}$C$^{16}$O ($J = 1\rightarrow0$) |
| Effective FWHP | 22″1 (378 pc) |
| Map grid spacing | 7″5 |
| Map size | $15.7 \times 16.9$ arcmin$^2$ |
| | ($16.1 \times 17.4$ kpc$^2$) |

\* On-source time calculated as number of scan rows × scan time.

the molecular gas in the nuclear region is driven in an outflow that takes the shape of an expanding cylinder, and encloses the H$\alpha$-emitting gas. Similarly, other observations of CO (e.g., Shen & Lo 1995; Seaquist & Clark 2001; Walter et al. 2002) have confirmed the presence of molecular gas outflow, and further uveiled its complexity.

Some of the most striking features related to the halo of M 82 are atomic hydrogen gas in the intergalactic medium around the galaxies of the M 81–M 82 group (e.g., Cottrell 1977; Appleton et al. 1981; Yun et al. 1994), H$\alpha$ filaments of ionized gas perpendicular to the major optical axis (e.g., Shopbell & Bland-Hawthorn 1998), UV and X-ray emission as far as 11 kpc above the galactic plane in the so-called Cap region (Hoopes et al. 2005; Tsuru et al. 2007, respectively), and a huge dust halo recently imaged with the AKARI and Herschel satellites (Kaneda et al. 2010; Roussel et al. 2010, respectively). Taylor, Walter, and Yun (2001) reported a large CO-gas halo, but the angular and velocity resolutions in their observations were insufficient to resolve the structure.

In this paper we present the results of the first high-resolution large-field mapping of the CO ($J = 1\rightarrow0$) halo in M 82. The paper is organized as follows. After this introduction, in section 2 we describe the observations and data reduction. It is followed by results in section 3: the distribution of CO gas and its motion revealed with the velocity field map. The results are discussed in section 4 while focusing on individual large-scale components of the molecular gas, namely the outflow, disk and streams. In the last part we compare the results with other data, particularly, concerning atomic gas (H I), vibrationally excited H$_2$, and emission from dust grains.

The basic parameters of M 82 adopted in this paper are summarized in table 1. Throughout this paper, we adopt the velocity with respect to the local standard of rest in the radio definition.

## 2. Observations and Data Reduction

The observations of $^{12}$CO ($J = 1\rightarrow0$) emission were made with the 45-m telescope of the Nobeyama Radio Observatory (NRO)[1] during 2009 March, 2010 February, April, and May.

---

[1] Nobeyama Radio Observatory is a branch of the National Astronomical Observatory of Japan, National Institutes of Natural Sciences.

The full width to half power (FWHP) of the main beam of the telescope was 15″ at the rest frequency of $^{12}$CO ($J = 1\rightarrow0$), 115.271204 GHz. In order to map a large portion of the sky ($15.7 \times 16.9$ arcmin$^2$) we employed the 25-Beam Array Receiver System (BEARS: Sunada et al. 2000) in the on-the-fly (OTF) mode. Details about OTF observations with the 45-m telescope were described in Sawada et al. (2008), and about the OTF in general in Mangum, Emerson, and Greisen (2007). OTF with BEARS provides simultaneous observations of 25 positions on the sky while the telescope is scanning at a constant speed. To correct for the scanning effects the map area was scanned in two directions perpendicular to each other. Maps in both directions were mosaics of four sub-maps, each covering one quarter of the total map, and the final map was created by coadding a total of 25 sub-maps (14 in X and 11 in Y direction, where X and Y refer to the major and minor axes of the galaxy, with a position angle of 65°). Since every single scan was completed in 37 s and 40 s along the X and Y axes, respectively, and one sub-map (with the scan separation of 5″) was completed in one hour, the weather conditions and system performance were stable during each observing run. The total time on the source was 15.2 hr, while the effective integration time on one cell of the final map was about 1 min. The system noise temperature in DSB (double side band) was $T_{\rm sys} = 390$ K on average [multiplied by a factor of about 2 to obtain the temperature in SSB (single side band)]. The receiver backend comprised 25 digital autocorrelation (AC) spectrometers (Sorai et al. 2000) with 1024 channels and a total bandwidth of 512 MHz, which corresponds to 1335 km s$^{-1}$ at 115 GHz. The calibration of the line intensity was made using an absorbing chopper wheel in front of the receivers, which yielded the antenna temperature, $T_{\rm A}^*$, corrected for the atmospheric and antenna ohmic losses (Ulich & Haas 1976). In this paper, we use the main beam brightness temperature, $T_{\rm mb} \equiv T_{\rm A}^*/\eta_{\rm mb}$, as the brightness temperature of CO. The main beam efficiency of the telescope was $\eta_{\rm mb} = 0.32 \pm 0.02$, as measured at 115 GHz by observing Mars, whose adopted brightness temperature was 210 K. In order to check and correct the positional error, reference pointing was conducted every $\sim 70$ min by observing the 43-GHz SiO maser line from a late-type star R-UMa; the pointing error was $\lesssim 4''$.

Data reduction was done by using the Nobeyama OTF Software Tools for Analysis and Reduction (NOSTAR) to
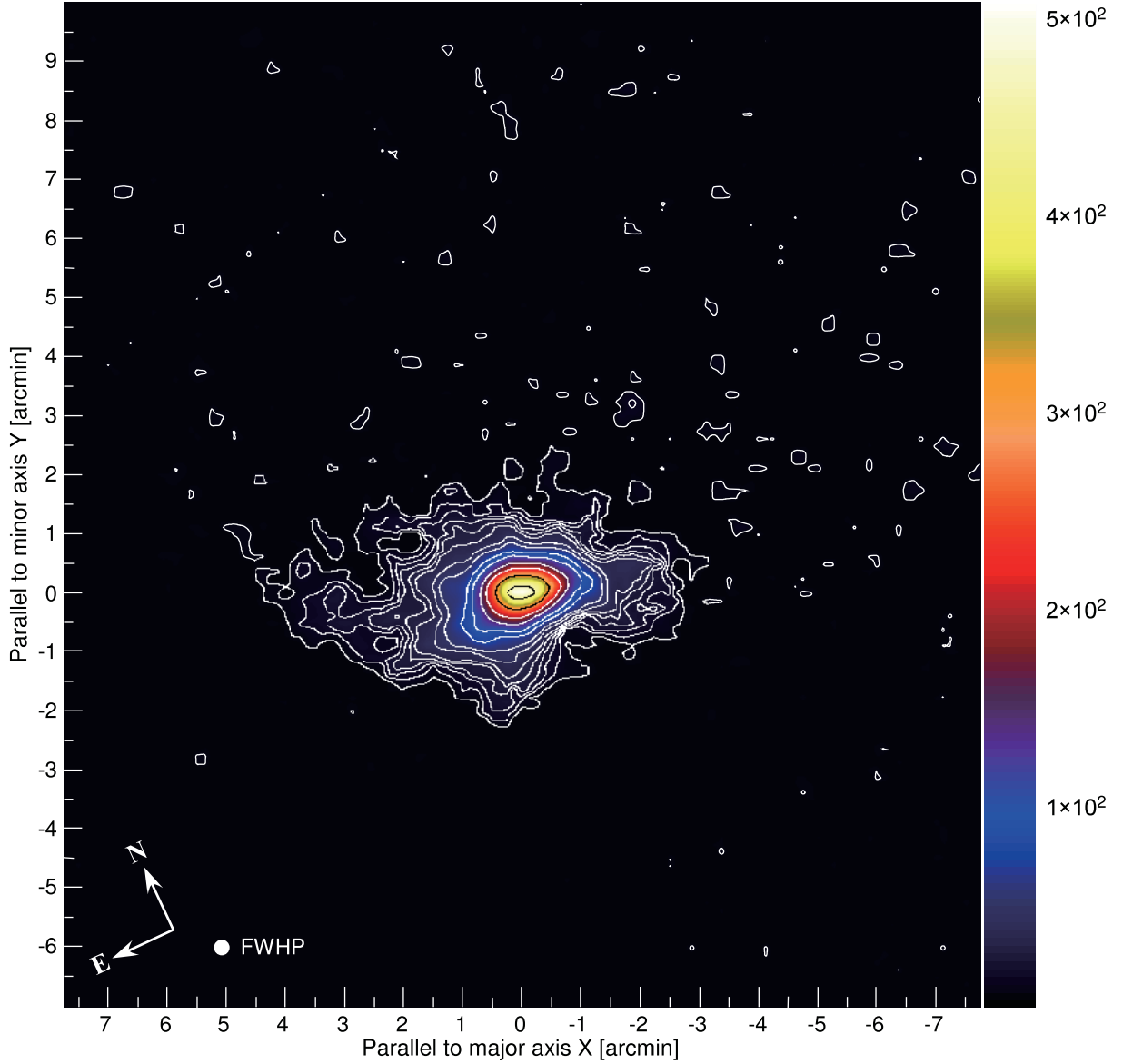
**Fig. 1.** Integrated intensity of the CO$(J = 1 \rightarrow 0)$ emission, $I_{\mathrm{CO}} = \int T_{\mathrm{mb}} dv$. The contours are 4, 10, 15, 20, 25, 30, 40, 50, 75, 100, 150, 200, 300, 450 K km s$^{-1}$. The axes of the map correspond to the optical major (X) and minor (Y) axes with a position angle of 65°. The scale of 1$'$ corresponds to 1.03 kpc at the distance of the galaxy, 3.53 Mpc. The effective spatial resolution (FWHP = 22$''$.1) is indicated at the bottom-left corner.

create a FITS file, and Astronomical Image Processing System (AIPS) to develop a 0-th moment map. The data were further analyzed and visualized by using the Interactive Data Language (IDL) and SAOImage DS9. During the NOSTAR phase, the reduction proceeded as follows. First we scaled the difference between two receiver sidebands (USB and LSB) by applying the correction scaling factors. Next, the baselines were fitted to a first-order polynomial and subtracted, while scanning rows were checked to flag bad spectra. During OTF scanning, data were acquired every 0.1 s, which corresponds to $\approx 2''.3$. To make a regular grid map, we convolved the data with a spheroidal function. This function increases the $S/N$ ratio at the cost of a larger effective beam size. The total observed area was X $\times$ Y = 1100$''$ $\times$ 1175$''$, but the area that was covered entirely by all 25 beams was $\approx$ 940$''$

$\times$ 1015$''$ (16.1 kpc $\times$ 17.4 kpc), and the grid spacing in the map was 7$''$.5, which was one half of the telescope beam. As a result, the effective beam size (FWHP) was 22$''$.1, corresponding to 378 pc at a distance of 3.53 Mpc. The average r.m.s. in a channel of a map pixel was 40 mK in $T_{\mathrm{mb}}$ when smoothed to a velocity resolution of 20 km s$^{-1}$. Details about observations and data reduction are summarized in table 2.

## 3. Results

### 3.1. Distribution of the CO Integrated Intensity

The CO$(J = 1 \rightarrow 0)$ integrated intensity is defined as $I_{\mathrm{CO}} \equiv \int T_{\mathrm{mb}} dv$, where the integration of the main beam brightness temperature, $T_{\mathrm{mb}}$, was done over velocities with emission detected mostly within $V_{\mathrm{LSR}} = 0$–450 km s$^{-1}$, around
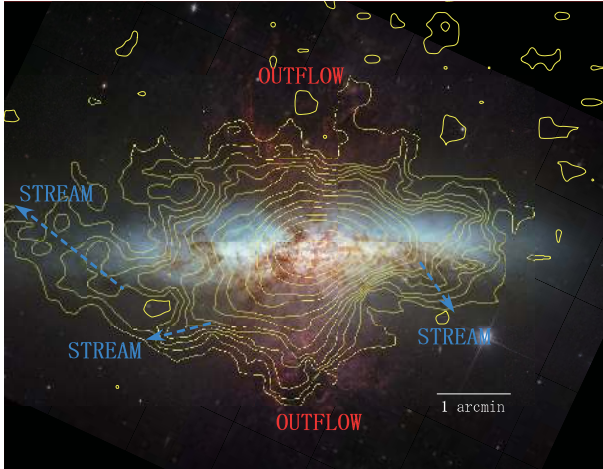
**Fig. 2.** Contours of the CO integrated intensity (figure 1) superimposed on an optical image (NASA, ESA, The Hubble Heritage Team). Blue arrows indicate molecular gas streams. The image is in XY coordinates (same as figure 1).

the adopted systemic velocity of $V_{sys} = 220\,\mathrm{km\,s^{-1}}$.

Figure 1 shows that the distribution of the CO intensity is predominantly strong in the central 500-pc region ($1' = 1.03\,\mathrm{kpc}$). The peak integrated intensity is $I_{CO} \simeq 507\,\mathrm{K\,km\,s^{-1}}$, but only 1 kpc from the center the intensity is as low as $50\,\mathrm{K\,km\,s^{-1}}$. Most of the halo emission has even lower intensities of $\sim 20\,\mathrm{K\,km\,s^{-1}}$. Therefore, the intensity drops rapidly outwards to an order of magnitude lower values. The uncertainty in the integrated intensity is expressed by $\Delta I_{CO} = \Delta T_{mb}\sqrt{\Delta v_{bin}\Delta v_{int}}$, where $\Delta T_{mb}$ is the noise level in the main beam brightness temperature per velocity bin, and the square root is taken from the width of the velocity bin, $\Delta v_{bin}$, and the integration range, $\Delta v_{int}$. Since they are $\Delta T_{mb} \simeq 40\,\mathrm{mK}$, $\Delta v_{bin} = 20\,\mathrm{km\,s^{-1}}$ and $\Delta v_{int} \lesssim 100\,\mathrm{km\,s^{-1}}$, the uncertainty is typically less than $\Delta I_{CO} \simeq 1.8\,\mathrm{K\,km\,s^{-1}}$.

By comparing with an optical image of the disk of M 82 (figure 2), we note that the overall distribution consists of three main distinct features: (1) the disk component—emission that lies along the optical major axis including the bright nucleus, (2) the outflow—remarkable extra-planar emission in the halo in the regions along the minor axis, and (3) the molecular gas streams, extending as far as 4 kpc from the inner regions. Additionally, we found patchy CO emission 3–4 kpc far from the galactic disk. Most of the patchy distribution deep in the halo has a significance of $3\,\sigma$ in $T_{mb}$, and might be noise. One of the patchy sites, shown with two contours in figure 1, has $4\,\sigma$; we return to that component in subsection 4.3.

The overall morphology of the CO distribution presented here has a number of features that can be related to previous large-scale observations (e.g., Taylor et al. 2001; Walter et al. 2002). The large-scale map in Taylor, Walter, and Yun (2001) revealed CO emission to a higher spatial extent. In addition to the unresolved central source, their CO integrated intensity map shows two large spur-like regions in the north and two smaller structures in the south. In the north, they detected a tidal arm in the north-east and an extended structure in the north-west. The eastern-most stream shown in this work

(figure 2) lies on the base of the tidal arm. Although the spur in the northwest is only sparsely traceable in our data, the presence of the NW clump (subsection 4.3) suggests that, in addition to the clump, there might be diffuse CO gas that was not detected in our observations. The patchy structures far on the southern side of the map in Taylor, Walter, and Yun (2001) were not detected either.

The high-angular resolution observations reported in Walter, Weiss, and Scoville (2002) revealed molecular gas streamers (named S1–S4 in their work) in the central region of M 82. Although these structures can be recognized only as spurs in figure 1 of this work, the location and shape of the streamers seem to be in good agreement in both data, taking into account the difference in angular resolution.

We made additional one-point observation towards the Cap region located $\sim 11\,\mathrm{kpc}$ above the plane of the galaxy. This region exhibits extended emission in X-ray (e.g., Lehnert et al. 1999; Stevens et al. 2003; Tsuru et al. 2007) and UV (e.g., Hoopes et al. 2005) thought to trace the hot gas ejected with the motion of the wind. Lallement et al. (2004) suggested that the origin of the X-ray emission in the Cap could be a charge-exchange process, where plasma is colliding with cool neutral clouds. We observed a point inside the X-ray emitting region where infrared emission observed with AKARI (Kaneda et al. 2010) has a peak, at $(\alpha, \delta)_{J2000.0} = (09^{h}55^{m}00^{s}, +69°50'15'')$ (outside the OTF map of figure 1). With a noise level of $\Delta T_{mb} \simeq 6\,\mathrm{mK}$, CO was not detected.

### 3.2. Large-Scale Kinematics of the CO Gas

In order to investigate the kinematics of the CO gas, we made a velocity field map (figure 3) and channel maps (figure 4). The peak velocities fall mostly in the range from $V_{LSR} = 110$ to $360\,\mathrm{km\,s^{-1}}$, whereas the total range of the CO line profiles spans from $V_{LSR} \simeq 0$ to $450\,\mathrm{km\,s^{-1}}$. With maximum rotation velocities of $\simeq 200\,\mathrm{km\,s^{-1}}$, M 82 has a relatively typical rotation for a disk galaxy. The kinematics of the molecular gas exhibits three main trends, as described below.

First, the nuclear region contains a torus or ring of dense gas rotating at a relatively high velocity of $200\,\mathrm{km\,s^{-1}}$. Its signature in the velocity field is a bright double peak around the central position of the map (see figures 3 and 9). The peaks are separated by $\simeq 0.4\,\mathrm{kpc}$, similarly to what has been observed in a number of previous studies (e.g., Nakai et al. 1987; Lo et al. 1987; Walter et al. 2002).

Second, outside the starburst region, which is within the inner 0.5 kpc along the X axis, in the plane of the galaxy, we find a larger thick disk of molecular gas rotating in the same sense as the central torus. The radial extent of the disk is $\sim 2'.5$ (2.5 kpc) in the X-axis (figure 1). The disk is roughly coincident with the stellar buldge (Ichikawa et al. 1995), and stretches outwards in a number of streams (figures 1 and 2), the innermost of them first reported in the high-resolution study of Walter, Weiss, and Scoville (2002) (streamers S1–S4). The structure of the molecular gas disk is better preserved in the western part of the disk, where the intensity distribution and velocities are fairly uniform; the blueshifted peak lies at $(X, Y) = (-1'.9, +0'.35)$ or $\simeq 0.36\,\mathrm{kpc}$ above the galactic plane (with the adopted P.A. of 65°). The eastern part of the CO disk is much less preserved, and seems to divide into
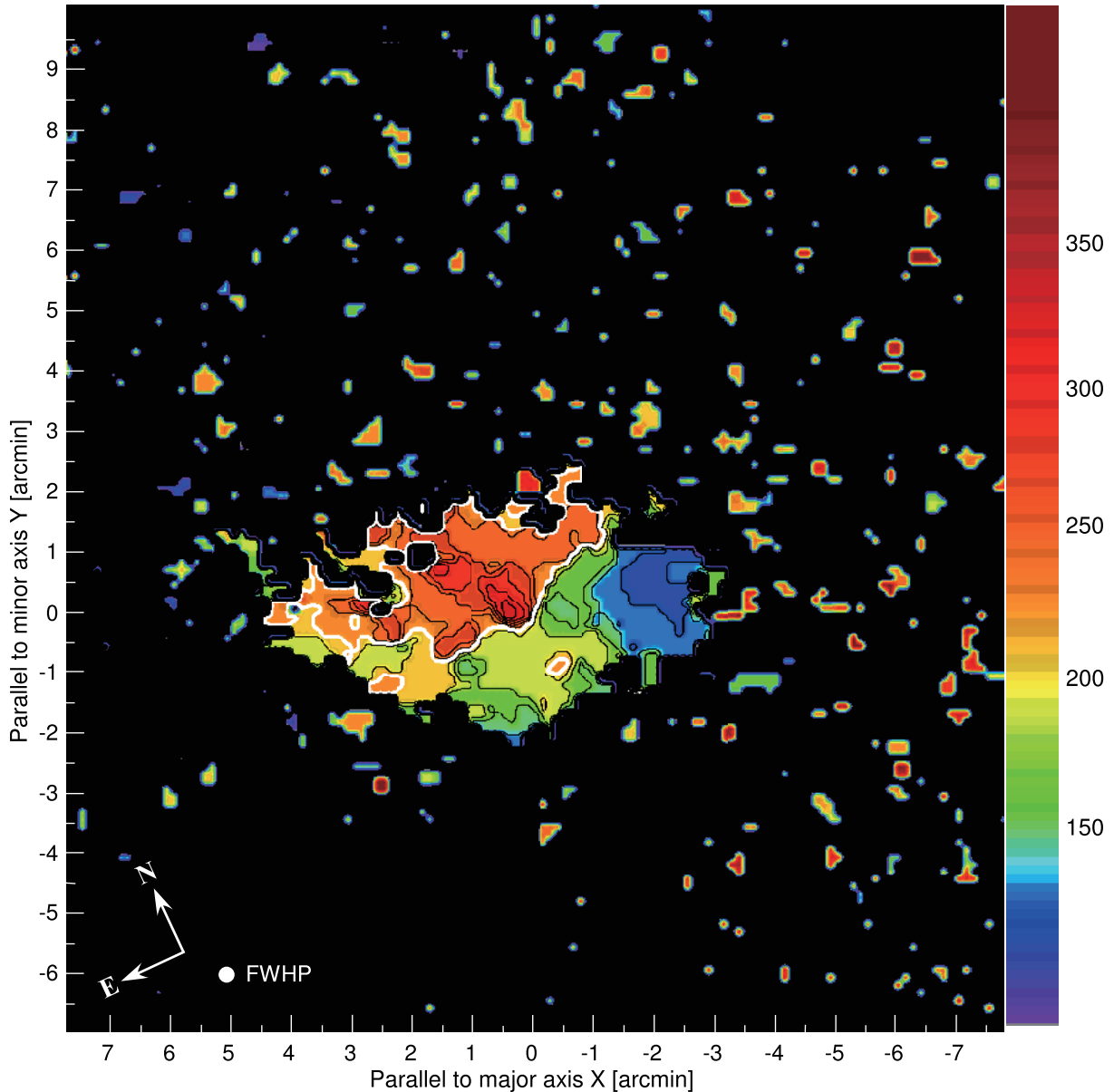
**Fig. 3.** Velocity field of the CO emission. The color bar is velocity $V$ in units $\mathrm{km\,s^{-1}}$, the white thick line marks the systemic velocity of $V_{\mathrm{sys}} = 220\,\mathrm{km\,s^{-1}}$ (Oloffson & Rydbeck 1984), and the black contours show isovelocity lines from $V = 100$ to $340\,\mathrm{km\,s^{-1}}$ separated by $20\,\mathrm{km\,s^{-1}}$.

two streams: a larger one towards the east, around (X, Y) = (+2′.0, −1′.0), and a smaller, narrower one towards the north-east, around (X, Y) = (+2′.0, +0′.5) (figure 2). Note that the larger stream has velocities near to the systemic velocity (denoted with white line in figure 3), and even blueshifted in some places, suggesting that the galactic rotation has been significantly disrupted there, and deviates from the rotation of the inner torus.

Third, the emission in the extra-planar regions near the minor galactic axis reveals a bi-conical molecular-gas outflow, as pointed out previously (e.g., Nakai et al. 1987). It reaches heights of at least 2 kpc in the north and south. The most important kinematical feature of the outflow is the difference in velocities of the northern and southern part; in the north we find predominantly redshifted, while in the south blueshifted

velocities with respect to the systemic velocity. This behavior is expected from the fact that M 82 is not exactly an edge-on galaxy, which will be discussed in the next section.

Figure 4 shows channel maps from 120 to $280\,\mathrm{km\,s^{-1}}$ with separations of $20\,\mathrm{km\,s^{-1}}$. Note a stream SE from the nucleus that is visible in all channels. In addition, at velocities from 180 to $240\,\mathrm{km\,s^{-1}}$, and especially at $200\,\mathrm{km\,s^{-1}}$, another stream that extends as a tidal arm (see below) is clearly resolved.

## 4. Discussion

The kpc-scale outflow of the molecular gas makes M 82 one of the nearest starburst galaxies with the molecular gas entrained in a prominent superwind. In this section we derive and discuss the properties of the main features: the outflow and
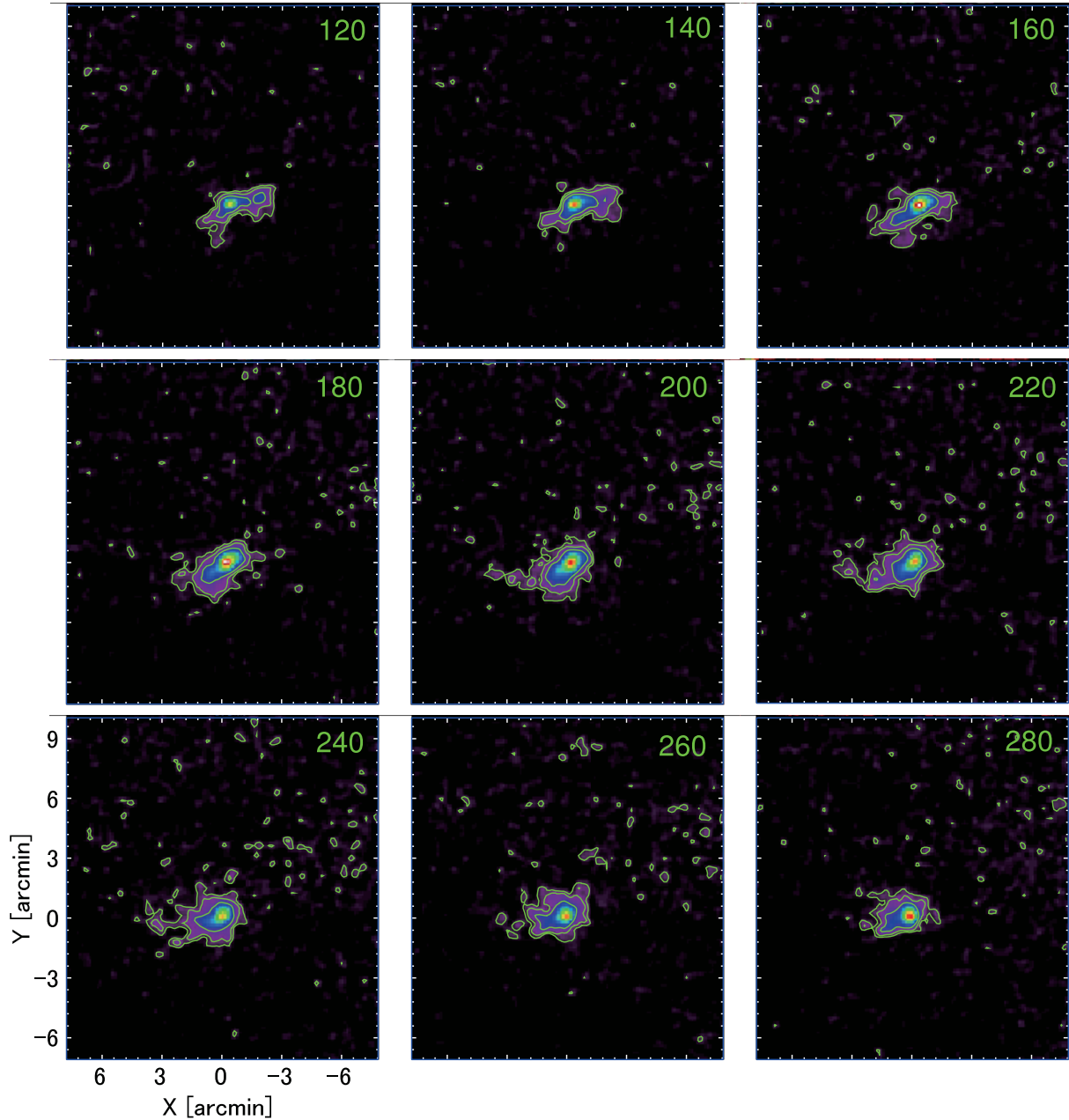
**Fig. 4.** Channel maps in the range $V_{\mathrm{LSR}} = 120\text{–}280 \, \mathrm{km\,s^{-1}}$. The contours are at $T_{\mathrm{mb}} = 0.13, 0.22, 0.44 \, \mathrm{K}$.

the tidal streams. In the last subsection we compare our results with other data.

### 4.1. Kinematics and Mass of the Outflow

By inspecting individual spectra in the data cube, we found that extra-planar regions where the spectra exhibit double peaks mark the boundary regions between the outflow and the disk emission. In figure 5 we show typical spectra along the boundary—the double peaks are interpreted as being two overlapping components. By searching farther in either direction parallel to the major axis, one of the components decreases and vanishes. In other words, within the outflow region, we

find that while spectra have blueshifted peaks in the south and redshifted peaks in the north, near the boudary regions another component appears, which gradually becomes dominant farther away from the outflow region. The composite spectra were fitted with two Gaussian functions wherever possible; the resulting outflow map is presented in figure 6.

In the northeast, notice that figure 3 shows a region with highly redshifted velocities ($\sim 300 \, \mathrm{km\,s^{-1}}$) extending from the nuclear torus in the NE direction. This feature is part of the disk, because, unlike all other streams, there is no prominent dust lane associated with it (see figure 2); it is more redshifted than the outflow, itself, with velocities not much different than
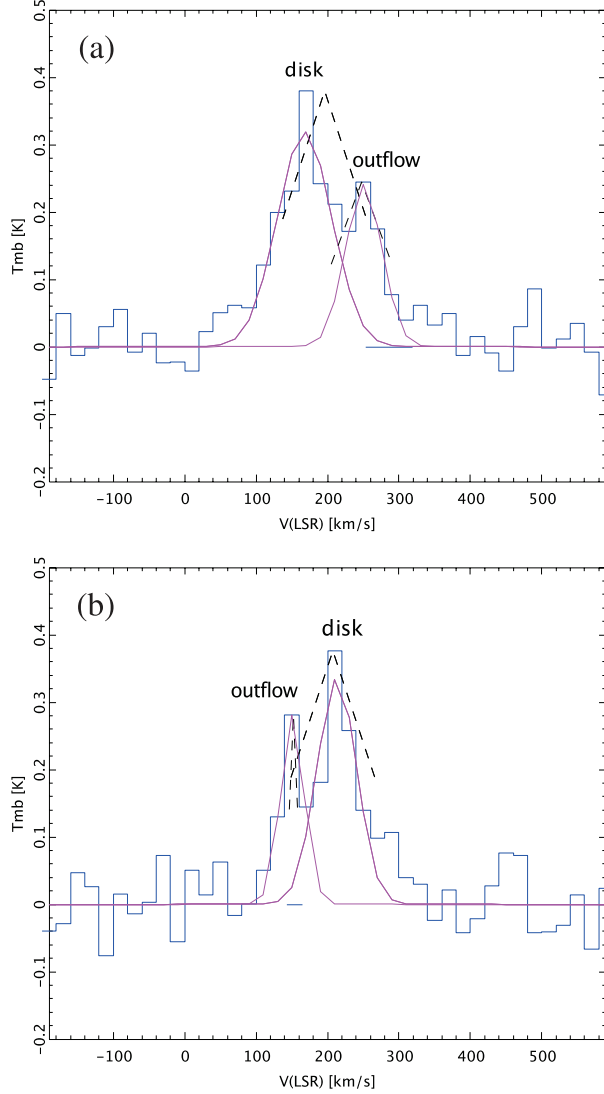
**Fig. 5.** Typical spectra (a) at $(X, Y) = (-37{.}''5, +37{.}''5)$ in the north, and (b) at $(X, Y) = (+82{.}''5, -67{.}''5)$ in the south—in regions where emission components from the outflow and from the disk/streamers overlap. The red lines indicate Gaussian fits.
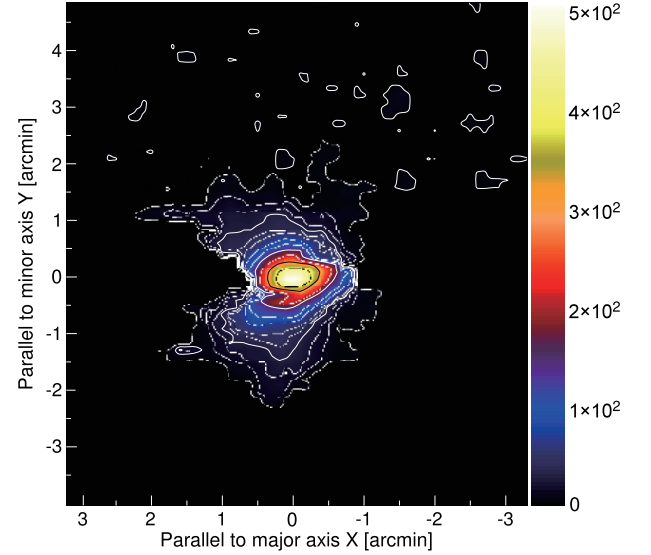


**Fig. 6.** Integrated intensity map of the outflow after subtracting the disk component (except for the nuclear region).

those in the eastern part of the nuclear torus.

In the central region we find broad lines (width $100$–$200\,\mathrm{km\,s^{-1}}$) and multiple components blended, which makes it difficult to decompose. Therefore, we adopt a boundary between the central disk and the outflow to be at $\pm 250\,\mathrm{pc}$ height from the galactic plane, and having a disk thickness of $500\,\mathrm{pc}$. This is presumably enough to account for any structures that may lie in the part of the disk between the central region and the observer, which are not part of the outflow. Additionally, note that the SE part of the outflow might be affected by the stream apparent in figure 4. The two components could not be clearly separated near the central region, and are treated as part of the outflow.

From the integrated intensity of the CO gas outflow (figure 6), we estimate the $H_2$ mass beyond $\pm 250\,\mathrm{pc}$ to be

$$M(H_2) = 2m_H A N(H_2) \simeq 1.0 \times 10^9\, M_\odot, \qquad (1)$$

where $m_H$ is the hydrogen atom mass, $A$ the map area of the emitting region, and $N(H_2)$ the column density of molecular hydrogen. In this calculation, a rather low Galactic CO-$H_2$ conversion factor, $X_{CO} \equiv N(H_2)/I_{CO} = 1.8 \times 10^{20}\,\mathrm{cm^{-2}\,K^{-1}}$ $(\mathrm{km\,s^{-1}})^{-1}$ (Dame et al. 2001), was adopted. If the same conversion factor is applied to the entire galaxy, we find the mass in the disk (including the nucleus) and streams to be $1.4 \times 10^9\, M_\odot$, and a total molecular gas mass of $2.4 \times 10^9\, M_\odot$. Thus, the molecular gas mass in the outflow could comprise as much as 40% of the total molecular gas mass in M 82. The resulting molecular gas mass is a considerable number for a relatively small and low-dynamical-mass galaxy ($\sim 10^{10}\, M_\odot$, Sofue 1998). For comparison, by using the above conversion factor, the total $H_2$ mass in the Milky Way is estimated to be $\sim 8.4 \times 10^8\, M_\odot$ (Nakanishi & Sofue 2006), and in M 31 it is only $\sim 3.6 \times 10^8\, M_\odot$ (Nieten et al. 2006), for a slightly larger conversion factor of $X_{CO} = 1.9 \times 10^{20}\,\mathrm{cm^{-2}\,K^{-1}\,(km\,s^{-1})^{-1}}$. In recent years, however, it has become evident that lower conversion factors are likely to be more realistic for starburst nuclei; for the nucleus of M 82 Weiss et al. (2001) obtained a low value of $X_{CO} = 0.5 \times 10^{20}\,\mathrm{cm^{-2}\,K^{-1}\,(km\,s^{-1})^{-1}}$ (also see Nakai & Kuno 1995). This is simply because a large kinetic temperature contributes to the increased integrated intensity of CO lines relative to the molecular gas column density, $N(H_2)$. The impact of the environment on $X_{CO}$ has been studied theoretically as well. In a recent study it was shown by numerical simulations that the conversion factor in luminous infrared galaxies should indeed be lower than the Galactic (Narayanan et al. 2012).

From the velocity information contained in the position–velocity (p–v) diagram (figure 7) we derived the outflow velocity of the molecular gas. After correcting for the inclination ($i = 80°$) and the opening angle [adopted to be $\theta = 60°$ as average from the literature: $40°$–$90°$ in Seaquist & Clark (2001); $55°$ in Walter et al. (2002)], the maximum projected velocity at $|Y| = 0{.}'5$ (figure 7), $|v_{p,max}| \simeq 160\,\mathrm{km\,s^{-1}}$,
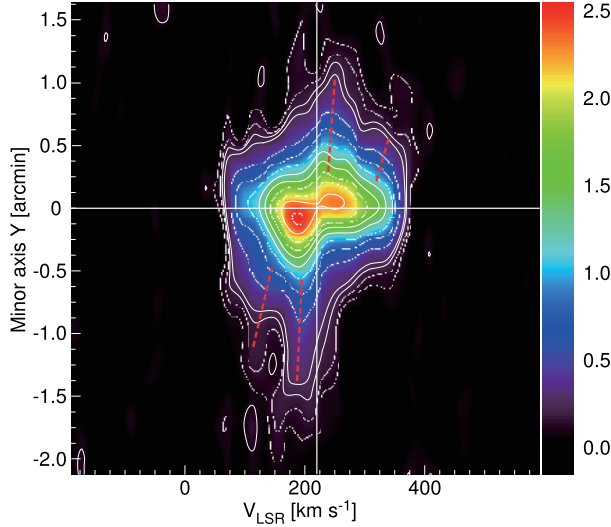
**Fig. 7.** Position–velocity diagram of the CO emission along the minor axis ($X = 0''$). The contours are $T_{mb}$ = 0.1, 0.15, 0.2, 0.25, 0.5, 0.75, 1.0, 1.25, 1.5, 1.75, 2.0, 2.25, 2.5, 2.75, 3.0 K, and the colorbar is $T_{mb}$ in K. The vertical white line marks the systemic velocity $V_{sys}$ = 220 km s$^{-1}$, and the red lines indicate line splitting. The scale of $1'$ corresponds to 1.03 kpc.

yields a maximum outflow velocity of $|v_{p,max}|/\sin(40°)$ $\simeq 250$ km s$^{-1}$. The maximum projected velocity beyond $0\rlap{.}''5$ above the galactic plane is $\sim 100$ km s$^{-1}$. This is lower than within $0\rlap{.}''5$ of the plane, and implies a deprojected velocity of $\simeq 155$ km s$^{-1}$. The average projected velocity above $0\rlap{.}''5$ is $\simeq 35$ km s$^{-1}$, which corrected for the inclination gives an outflow velocity of $\simeq 200$ km s$^{-1}$. We adopt $v_{out} = 200$ km s$^{-1}$ as the outflow velocity. With the mass estimate in equation (1), the kinetic energy of the molecular gas in the outflow is $E_k = M(\mathrm{H_2})v_{out}^2/2 \sim 4 \times 10^{56}$ erg. In the low-$X_{CO}$ case of Weiss et al. (2001), the energy is $\sim 1 \times 10^{56}$ erg. If one supernova explosion releases $E_0 = 10^{51}$ erg in the form of kinetic energy, and the recent starburst event has lasted for $t_{SN} \sim 5 \times 10^7$ yr (O'Connell et al. 1995), following the starburst model in Rieke et al. (1980); assuming a constant supernova rate, $\mathcal{R}_{SN} = 0.09$ yr$^{-1}$ (Fenech et al. 2010), the kinetic energy released by supernova explosions is

$$E_{SN} = \mathcal{R}_{SN} t_{SN} E_0 \simeq 5 \times 10^{57} \text{ erg.} \qquad (2)$$

Hence, at least 2% of the supernova energy released in the ISM is transferred to the molecular gas, but the number could be as high as 8%, depending on the conversion factor. The derived kinetic energy, $E_k$, is an order of magnitude higher than estimated by Nakai et al. (1987), and a factor of 3 higher than in Walter, Weiss, and Scoville (2002). In the former the mass estimate was much lower because of the limitation of the CO-mapping area ($90'' \times 90''$), whereas in the latter the adopted outflow velocity was lower (100 km s$^{-1}$), estimated from their p–v diagram, which traces emission within $\pm 50''$ from the galactic center.

The kinetic energy, $E_k$, is two orders of magnitude higher than that of the ionized gas, which is $\sim 2 \times 10^{55}$ erg (Shopbell & Bland-Hawthorn 1998), and three orders of magnitude higher than that of the dust grains and polycyclic aromatic
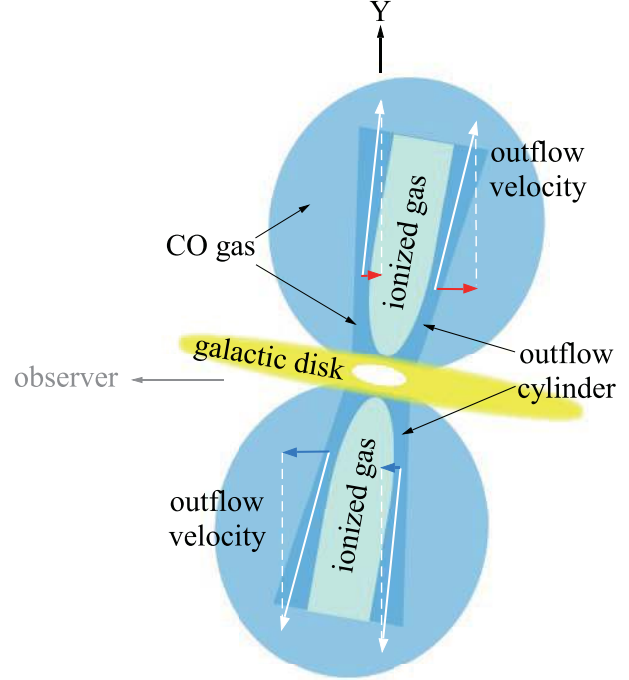


**Fig. 8.** Outflow model. CO emission arises mostly from a cylinder perpendicular to the galactic plane. Inside the cylinder the gas is mostly ionized, whereas outside it is mostly neutral.

**Table 3.** Parameters of the molecular gas outflow.

| | |
|---|---|
| Mass* | $(0.26$–$1.0) \times 10^9 \, M_\odot$ |
| Opening angle† | $60°$ |
| Velocity‡ | 200 km s$^{-1}$ |
| Kinetic energy* | $(1$–$4) \times 10^{56}$ erg |

\* For the conversion factor $X_{CO} = (0.5$–$1.8) \times 10^{20}$ cm$^{-2}$ (K km s$^{-1}$)$^{-1}$.
† Average from the literature (see text).
‡ For the inclination angle $i = 80°$.

hydrocarbons (PAHs), if they share the same kinematics as the molecular gas, whose total mass is $\sim 10^6 \, M_\odot$ (Kaneda et al. 2010). In fact, the velocities of the dust component were estimated to be comparable, but somewhat lower (between 100 and 200 km s$^{-1}$, assuming that the galactic inclination is 75°) than that of the molecular gas; it is interesting to note that the dust velocity is measured to be *decreasing* with distance along the minor axis (Yoshida et al. 2011), whereas our data suggest no such trend for the CO gas.

The spurs in the p–v diagram (dotted red lines in figure 7) indicate line splitting. This feature was first reported in Walter, Weiss, and Scoville (2002), but our data show that both components of the splitted line can be seen at least up to $-80''$ in the south, and a similar but redshifted pattern appears in the north up to $+60''$. Note, however, that the p–v diagram in Walter, Weiss, and Scoville (2002) is at P.A. = 150°, and ours is at P.A. = 155° (minor axis). The minor axis, Y, is used here because figure 6 shows no preferred direction for the outflow other than Y, which could be adopted for both north and south.
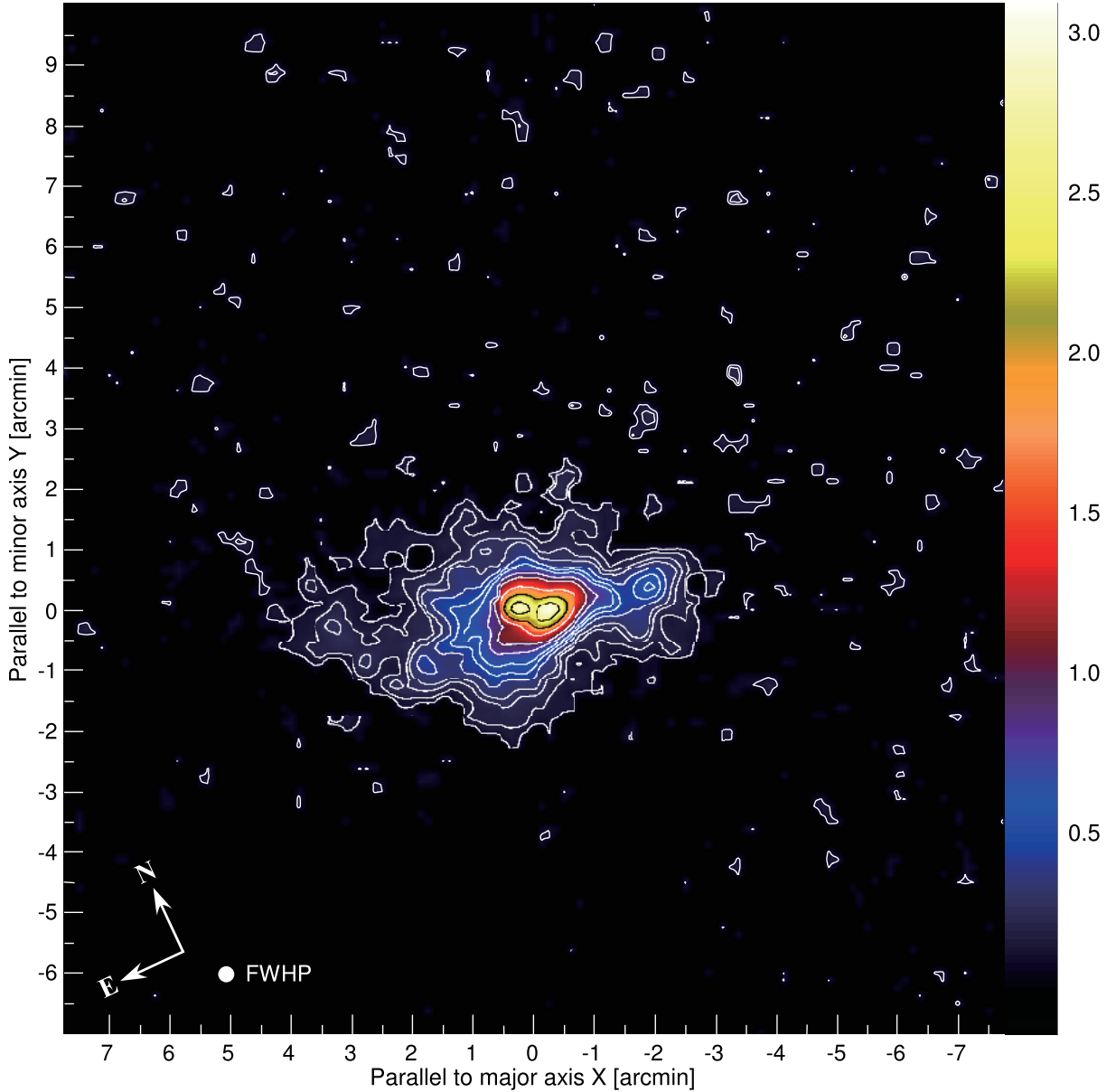
**Fig. 9.** Main beam brightness temperature map. The contours are $T_{mb} = 0.12, 0.18, 0.25, 0.3, 0.4, 0.5, 0.6, 0.8, 1.0, 1.5, 2.0, 2.6$ K. The colorbar is $T_{mb}$ in units K.

In addition, there is an indication of minor line splitting in the blueshifted velocity domain in the northern part of the outflow at $-30$, $-100$, and $-150\,\mathrm{km\,s^{-1}}$ with respect to the systemic velocity. A similar feature at $-100\,\mathrm{km\,s^{-1}}$ was also discovered at optical wavelengths [figure 10 in Shopbell & Bland-Hawthorn (1998)], and can be traced only in the north. The molecular gas may be entrained with the ionized gas in this component.

The splitting suggests that most of the gas is confined to a cylindrically shaped outflow with low inclination with respect to the minor axis; this is illustrated in figure 8. The peaks in the p–v map, such as those near the points $(Y, v) = (-1.0\,\mathrm{kpc}, 120\,\mathrm{km\,s^{-1}})$ and $(+1.0\,\mathrm{kpc}, 380\,\mathrm{km\,s^{-1}})$, can be interpreted as projections of the velocity components belonging to the walls of the outflow cylinder along the line of

sight. Outside this main structure we find a divergent component that is reflected with a boarder range of velocities in the outflow region in the p–v map. The parameters of the molecular gas outflow are summarized in table 3.

### 4.2. The Thick Disk and Streams

Figure 9 shows the distribution of the CO emission where the integrated intensity is replaced with the main beam brightness temperature, $T_{mb}$, of the peaks in the spectra. Although the overall distribution is similar to that of the integrated intensity (figure 1), we distinguish additional sub-structures. The nucleus is resolved into two bright peaks, revealing the nuclear ring (Nakai et al. 1987). In the galactic plane we find an irregular and thick molecular gas disk, with its east part divided into two main streams, at $(X, Y) = (+2\farcm0, -1\farcm0)$

and (X, Y) = (+2′.0, +0′.5), gradually increasing their extra-planar height away from the nucleus. These streams were first reported in Walter, Weiss, and Scoville (2002) as S4 and S2, respectively, along with a similar structure seen in the western part too, labeled S1, shifting below the plane at (X, Y) = (−1′.75, −0′.25). From figure 2 we notice that these streams correlate well with dark dust lanes. The origin of these lanes is discussed in Ohyama et al. (2002). From the CO data we can understand that some of the dust lanes and CO gas are part of the same galactic streams emerging from the central region, and bending in a similar fashion.

The easternmost stream in figure 2 appears to lie on the base of a large tidal arm revealed in Taylor, Walter, and Yun (2001). This feature was observed to a much larger extent in H I as well (see subsection 4.4), and the structure in our map is the inter-region between the inner streamer labeled S4 in Walter, Weiss, and Scoville (2002) and the tidal arm in Taylor, Walter, and Yun (2001).

In the western part of the disk, at (X, Y) = (−1′.9, +0′.4), we have discovered a new peak above the galactic plane, with the highest blueshift in the western part of the disk (peak velocity at $-110 \, \mathrm{km \, s^{-1}}$ relative to $V_{\mathrm{sys}}$). Its nature could be a stream along the line of sight, but a more plausible explanation is that this structure is part of a spiral arm, proposed by Mayya, Carrasco, and Luna (2005), and the peak is where the arm is in the line-of-sight direction. Mayya, Carrasco, and Luna (2005) investigated the near-IR emission from the disk, and also found a peak in this region, which was modeled as one of the $m = 2$ spiral arm pattern.

It is noteworthy that bursts of star formation throughout the disk of M 82, which have most recently happened 0.8 Gyr ago and lasted for 0.3 Gyr (Mayya et al. 2006), have increased the released energy (stellar winds and supernova explosions), and may be responsible for the formation of the thick disk of diffuse molecular gas. Otherwise, it would be difficult to explain its large scale heights (nearly 2 kpc thick), since the streamers are smaller than this, and the galactic wind/outflow has been found to emerge mostly from the nuclear region. In addition, continuum emission from dust grains (subsection 4.4) reveals a spherical dust halo; the origin of all of this dust is difficult to trace back to the central 0′.5, which is the size of the nuclear starburst, or to tidal interactions which have created distinct tidal arms of atomic gas. It is more likely that a larger part of the disk of M 82 was to some extent involved in the ejection of the material into the halo. In the scenario of a disk-wide starburst, rapid consumption of molecular gas would eventually suppress further star formation, and leave a relatively quiescent disk immersed in a thick layer of gas and dust. A similar outcome has been obtained in recent numerical simulations (Hopkins et al. 2012), where dwarf starburst galaxies exhibit dusty, thick and irregular disks, a bar in the nucleus and galactic winds. We find M 82 to be suitable for the Sbc-type in their simulation. The origin of the disk-wide starburst, on the other hand, can be explained by past tidal interactions, with the interactions from 1 Gyr ago and the latest close encounter happening 0.3 Gyr ago (Yun et al. 1994; Sofue 1998).

The presence of a thick disk is most apparent in the western side of the galaxy where the CO emission was detected up to 1 kpc above the galactic plane (maxima at Y = +1′.0 in
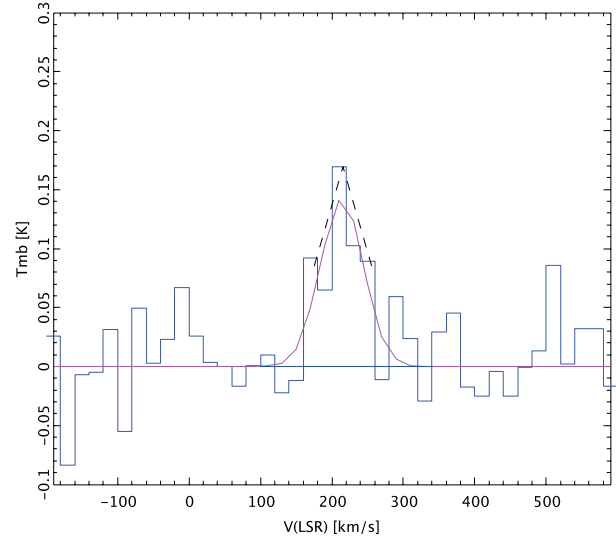


**Fig. 10.** Spectrum taken over a region of $15'' \times 15''$ centered at the peak of the NW clump. The red line is a Gaussian fit.

**Table 4.** Parameters of the CO emission at the peak of the NW clump.

| | |
|---|---|
| $T_{\mathrm{mb}}$ | $142 \pm 34 \, \mathrm{mK}$ |
| $V_{\mathrm{c}}$ | $214 \pm 10 \, \mathrm{km \, s^{-1}}$ |
| $I_{\mathrm{CO}}$ | $10.7 \pm 1.9 \, \mathrm{K \, km \, s^{-1}}$ |
| Line FWHP | $71 \pm 15 \, \mathrm{km \, s^{-1}}$ |

the north and Y = −0′.8 in the south). This feature includes the above-mentioned peak, which was not detected in Walter, Weiss, and Scoville (2002). The reason for that might be the fact that the feature is rather extended, to which interferometers are less sensitive. Also, the peak of this extended emission at (X, Y) = (−1′.9, +0′.4) is 2′ from the galactic center, which is at the edge of their mosaic map. On the other hand, streamer S1 in Walter, Weiss, and Scoville (2002) is only ∼ 0′.5 thick, and can be recognized in figures 2 and 9 as a spur in the SW direction, coincident with a dust lane.

### 4.3.  The North-West Clump

In the northern side of the halo, at (X, Y) = (−1′.85, +3′.25) or $(\alpha, \delta)_{\mathrm{J2000}} = (9^{\mathrm{h}} 55^{\mathrm{m}} 19^{\mathrm{s}}.0, +69°42'50''.0)$, we found a patch of CO emission (hereafter referred to as the "NW clump") with a significance of $4\sigma$ in $T_{\mathrm{mb}}$. This feature is most likely to be real, beacuse a comparison with other data shows that there is also a peak in H I emission (see figure 11 in subsection 4.4). A spectrum centered on the CO peak in this region, integrated over an area of $15'' \times 15''$, is shown in figure 10, and the properties of the Gaussian-fitted line are listed in table 4.

The average integrated intensity over the clump region where CO emission was detected with $S/N \gtrsim 3\sigma$ (diameter ∼ 30″ or 0.5 kpc) is $I_{\mathrm{CO}} = 8.9 \, \mathrm{K \, km \, s^{-1}}$. The CO-$H_2$ conversion factor is virtually unknown for the extreme environment where this emission arises from, but for a range of factors in the literature, $X_{\mathrm{CO}} = (0.5\text{–}2.0) \times 10^{20} \, \mathrm{cm^{-2} \, K^{-1} \, (km \, s^{-1})^{-1}}$, we estimate that the average column density of $H_2$ is $N(H_2) = (0.4\text{–}1.8) \times 10^{21} \, \mathrm{cm^{-2}}$. Using equation (1), this gives a range

of molecular gas masses of $M(H_2) = (1.6–7.2) \times 10^6\,M_\odot$. This estimate is very rough, though, because there may be a substantial quanity of $H_2$ not associated with CO emission, and the physical conditions of the gas are unknown.

H I column densities in the region are estimated to be $N(\mathrm{H\,I}) \simeq (0.2–1.1) \times 10^{21}\,\mathrm{cm^{-2}}$ (Yun et al. 1993, 1994), which is similar to that for CO, and implies a total column density of $N_\mathrm{H} \equiv N(\mathrm{H\,I}) + 2N(\mathrm{H_2}) \simeq (1.0–1.9) \times 10^{21}\,\mathrm{cm^{-2}}$, where the low conversion factor is applied. This value of $N_\mathrm{H}$ is fairly large, and similar to the column densities in photodissociation regions, at dissociation fronts where H and $H_2$ coexist in comparable proportions in diffuse/translucent media (e.g., Snow & McCall 2006; Draine 2011).

The origin of the clump is difficult to determine from the CO data alone. Note that the center of the line, $V_c = 214\,\mathrm{km\,s^{-1}}$, is near the adopted systemic velocity of M 82, $V_\mathrm{sys} = 220\,\mathrm{km\,s^{-1}}$. This indicates that the clump might be in motion perpendicular to the line of sight. Such motion is expected from the nearby outflowing material, but it could also be of tidal origin. X-ray observations reported in Stevens, Read, and Bravo-Guerrero (2003) have revealed a "dark lane" in the region of the NW clump, an unusual bridge where the X-ray emission from the outflow plasma is faint, whereas the H I intensity increases. There are two possibilities to explain the anticorrelation: (1) intervening material absorbing soft X-rays, or (2) interaction between the X-ray emitting plasma with the ambient gas. Tsuru et al. (1997) have pointed out that low brightness in the 0.5–0.8 keV X-ray image was coincident with the molecular gas disk of M 82. On the other hand, Stevens, Read, and Bravo-Guerrero (2003) have found no hardening in the X-ray spectra towards the dark lane, suggesting that both absorption and interaction might be important. In either case, the atomic and molecular gas could play the role of the ambient material, and since no such anticorrelation between the neutral gas and X-ray emission is seen in other parts of the outflow, where the neutral gas is entrained in the superwind, we favor the interpretation of a tidal origin for the NW clump and the corresponding dark lane.

### 4.4. Comparison with Data on Other Wavelengths

#### 4.4.1. Ratio of CO(3–2) and CO(1–0)

Owing to its proximity and high inclination, M 82 is a very useful target to study different environments of the ISM—the starburst nucleus, outflow and molecular gas streams. The physical parameters of the molecular gas in the central region of M 82 were studied in a number of previous studies (e.g., Seaquist & Clark 2001; Weiss et al. 2005), which demonstrated the importance of a multi-line approach. In this context, we derived a $2 \times 2\,\mathrm{arcmin^2}$ ratio map of the CO integrated intensity from this work and $I_\mathrm{CO}(J = 3{\to}2)$ from Seaquist and Clark (2001), defined as $R_{31} \equiv I_\mathrm{CO}(J = 3{\to}2)/I_\mathrm{CO}(J = 1{\to}0)$ (figure 11a). The intensity maps were corrected for the difference in the angular resolution and the channel width.

The line ratio is high ($R_{31} \gtrsim 1.0$) in the starburst nucleus, and decreases gradually outwards down to $R_{31} = 0.5 \pm 0.2$ at $Y = +30''$ and $Y = -40''$. The decline is more rapid along the minor axis compared to the major axis, where it retains a value of 0.7 up to $|X| = 50''$ east of the nucleus. (figure 11b). This tendency is in agreement with previous measurements of
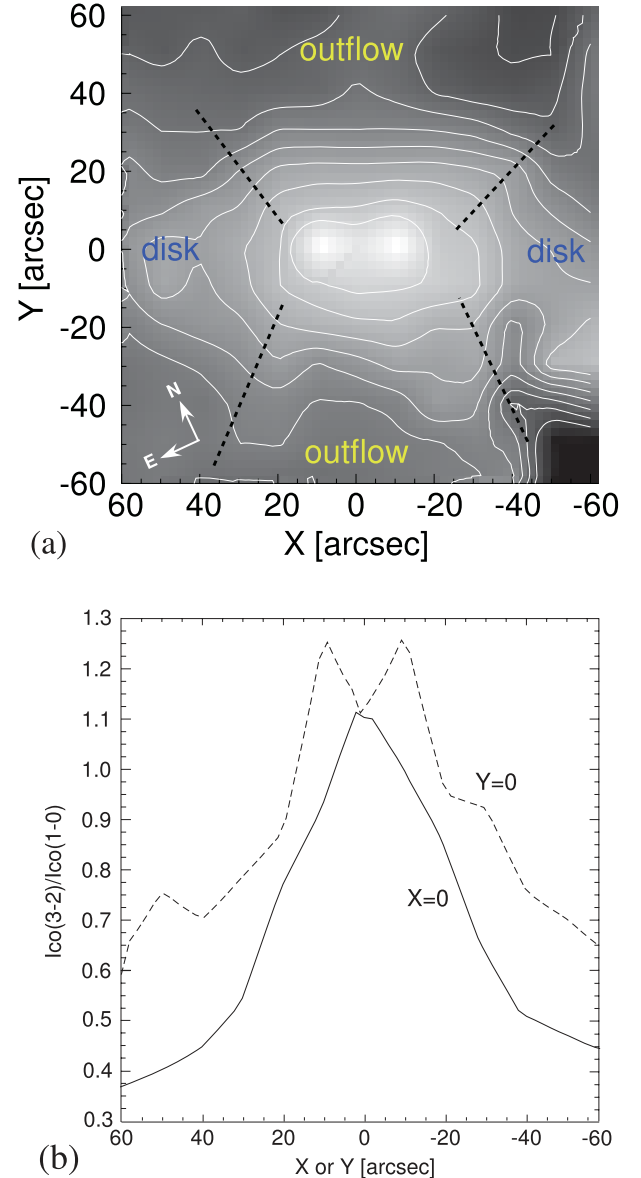


**Fig. 11.** (a) Ratio map of the integrated intensity $R_{31} = I_\mathrm{CO}(3–2)/I_\mathrm{CO}(1–0)$, and (b) profiles along X and Y axes. The highest contour in the nucleus is at $R_{31} = 1.0$, and the contour interval is 0.1.

the line ratios in Weiss, Walter, and Scoville (2005), where it was found that the ratios are higher in the disk and streams than in the outflow.

The gradual decrease in $R_{31}$ along the minor axis in the outflow suggests that the physical conditions of the molecular gas are not constant throughout the outflow. The $CO(J = 3{\to}2)$ line is a tracer of warm and/or dense gas in which collisions populate the $J = 3$ rotational energy level. Beyond $|Y| = 40''$ we find $R_{31} \lesssim 0.5$, which clearly reflects decreasing excitation with distance from the central region.

#### 4.4.2. Atomic hydrogen

M 82 is a member galaxy of a larger system including M 81, NGC 3077, and a number of smaller galaxies. Observations of the 21-cm line of H I (Cottrell 1977; Appleton et al. 1981;
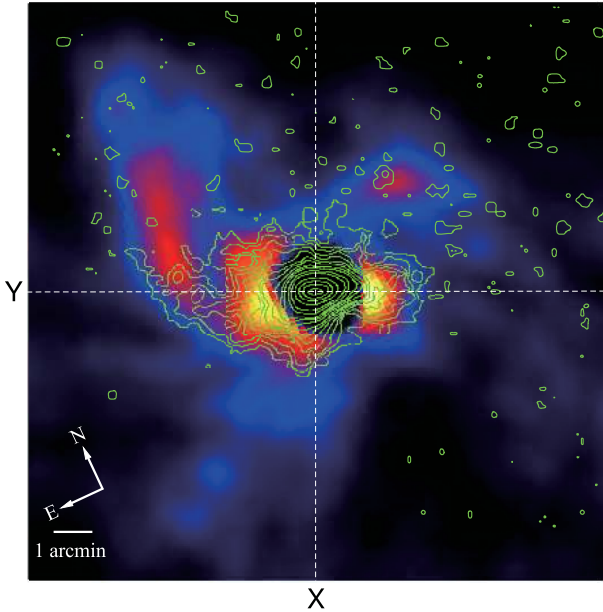
**Fig. 12.** Superposition of the CO $(J = 1\rightarrow0)$ integrated intensity (contours) on the H I 21-cm integrated intensity map (color) from Yun, Ho, and Lo (1994).



**Fig. 13.** Superposition of CO $(J = 1\rightarrow0)$ integrated intensity (contours) on the 2.12-$\mu$m molecular hydrogen image (color) from Veilleux, Rupke, and Swaters (2009), where the flux scale is in units erg s$^{-1}$ cm$^{-2}$ arcsec$^{-2}$.

Yun et al. 1994; Chynoweth et al. 2008) have revealed giant filaments of atomic gas connecting these three largest members. The structure is thought to have formed in tidal interactions during close-approach events within the past 1 Gyr. Taylor, Walter, and Yun (2001) have reported that the molecular gas is driven into the tidal arm around M 82, which extends several kpc toward NE. Figure 12 shows a superposition of the CO contours from our work (figure 1) on an H I image from Yun, Ho, and Lo (1994). We note resemblence in the two distributions in the central 3′ and that the easternmost CO stream is part of the tidal arm. On the other hand, although the distributions in the inner regions seem to correlate well, H I absorption and low angular resolution ($\approx 60''$) of the H I map makes it difficult to probe the structure near the galactic plane. As discussed above, the NW clump of CO gas $\sim 4$ kpc north-west from the nucleus (subsection 4.3) is also a bright peak in H I.

### 4.4.3. Hot molecular hydrogen

When the physical state of molecular hydrogen gas satisfies certain conditions, vibrational and rotational levels above the ground state become significantly populated. At high densities and temperatures, and in shocked regions, the upper states are popluted via collisional excitation; in less dense regions, intense UV fields may be a more effective mechanism. At least one of these conditions is likely to be satisfied in the outflow of M 82. Observations of the molecular hydrogen $H_2$ $v = 1$–0 $S(1)$ line at the near-IR wavelength of 2.12 $\mu$m (Veilleux et al. 2009) have revealed significantly enhanced emission in the outflow, in a shape of filaments, as well as bright emission from the galactic disk and nucleus.

Unlike the rovibrational transitions of hydrogen, however, rotational transitions of CO arise in both warm and cold ("undisturbed") molecular clouds. Hence, by comparing the dis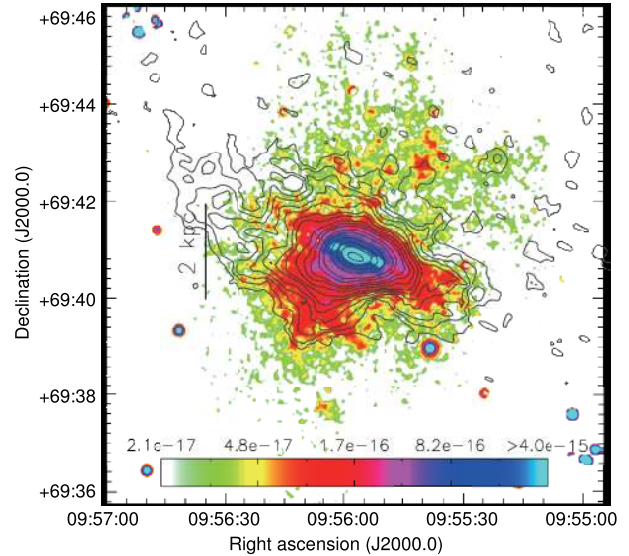tributions of the two we may trace the physical conditions throughout the molecular hydrogen gas. Figure 13 shows the overlap of the CO and $H_2$ maps. Although the overall structure of the two maps is similar, details are different: the near-IR emission from $H_2$ is relatively brighter than the CO in the outflow, at $\delta_{J2000.0} \gtrsim 69°43'$, compared to the eastern tidal stream, at $\alpha_{J2000.0} \gtrsim 9^h56^m30^s$, where CO was detected, but $H_2$ was not.

The contrast found in the outflow and the tidal stream can be explained by considering the excitation mechanisms. In the outflow, the gas is likely to be exposed to at least two effects: shocks within the entrained structures of the wind-blown material, and the UV field coming from hot stars in the galactic plane. It has been known that galactic winds increase the porosity of the ISM (Veilleux et al. 2005), and the nucleus of M 82 hosts one of the strongest UV fields in the nearby universe with far-UV emission detected more than 5 kpc above the galactic plane (Hoopes et al. 2005). This emission is observable due to the scattering of UV photons on dust grains, and shows that the outflow region is highly exposed. On the other hand, diffuse CO gas is more easily destroyed via photodissociation than $H_2$, and survives only in dense media where shielding is effective (van Dishoeck & Black 1988). One such candidate place is the NW clump discussed above, as an extra-planar photodissociation region.

In the case of the tidal streams, the molecular gas has been pulled from its original place by gravity during a previous encounter with M 81 (Yun et al. 1994). It consists of cold molecular gas co-existing with atomic gas and dust, far from the central starburst, and hence beyond the reach of the UV field from its hot stars.

### 4.4.4. Dust grains

Continuum emission from dust grains has been observed at various wavelenghts, from cold in the millimeter regime (e.g., Thuma et al. 2000), cool in the sub-mm (Roussel et al. 2010) to

warm components including PAHs in the near-IR (Engelbracht et al. 2006; Kaneda et al. 2010). In figure 14 we show a superposition of the CO emission contours on the $250\,\mu$m map of cool dust obtained with SPIRE onboard the Herschel satellite (Roussel et al. 2010).

Dust emission is detected to a higher extent than CO in this work, although it seems from figures 14 and 15 that the two share several extra-planar features. In addition to a fairly good correlation in the central region, most obviously, both molecular gas and dust are enhanced in the eastern tidal stream. As discussed above, we conclude that this feature contains relatively cool interstellar matter. In figure 15 we show an overlap of the contours of the $7$-$\mu$m emission from warm dust grains and PAHs (Kaneda et al. 2010) on the image of the CO ($J = 1{\to}0$) integrated intensity. In order to investigate whether the change of the intensities of CO and warm dust along the galactic major and minor axes is alike, we derived normalized profiles from data cubes corrected for the angular resolution difference (figure 16). As expected, the decreasing tendency is sharper along the Y axis, which is similar between CO and dust. However, the dust intensity decreases more sharply than that of CO. There is some similarity
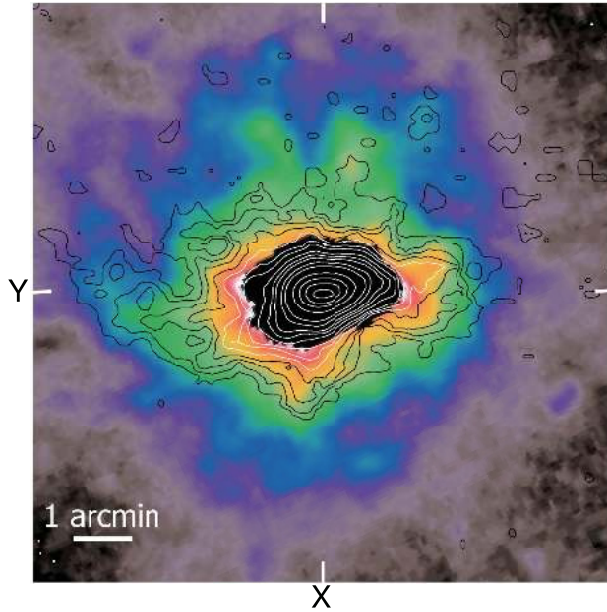


**Fig. 14.** Superposition of the CO ($J = 1{\to}0$) integrated intensity (contours) on the $250$-$\mu$m dust emission (flux density) image (color) obtained with Herschel (Roussel et al. 2010). The map size is 10 $\times$ 10 arcmin$^2$.



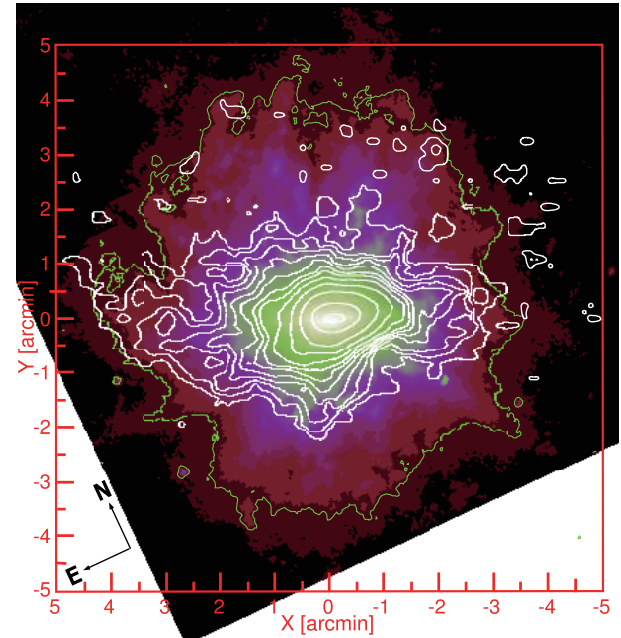**Fig. 15.** Contours of the integrated intensity of CO ($J = 1{\to}0$) superimposed on the image of the $7$-$\mu$m map from Kaneda et al. (2010). The green contour is at $0.3$ MJy sr$^{-1}$ ($0.007\%$ of the peak) of the dust image.
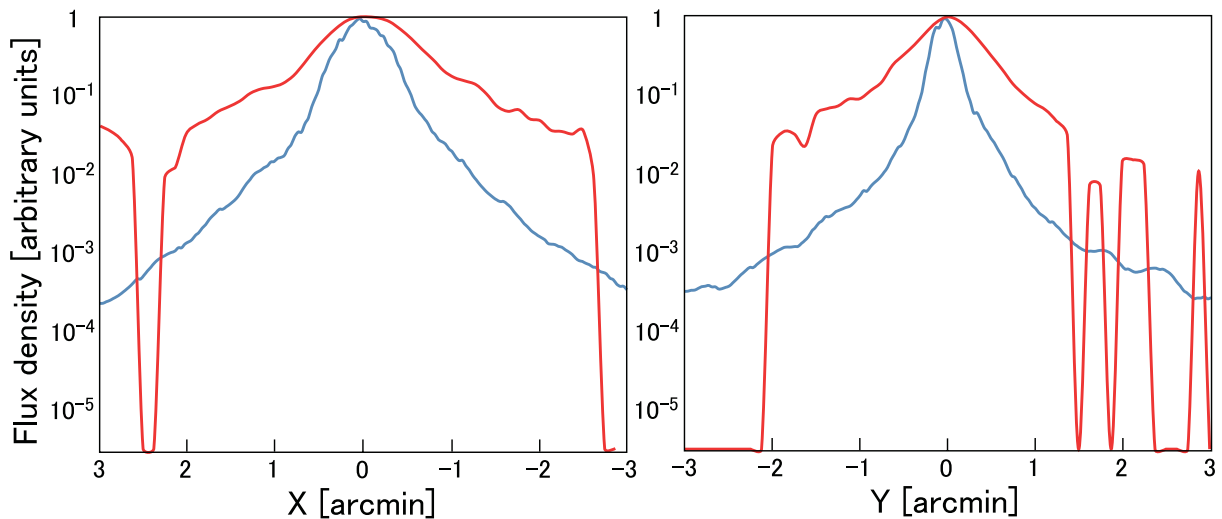


**Fig. 16.** Normalized intensity of CO ($J = 1{\to}0$) from this work (red line) and dust at $7\,\mu$m from Kaneda et al. (2010) (blue line) along the major (Y = 0″) and minor (X = 0″) axes plotted on a logarithmic scale.

between this comparison and the results given in Thuma et al. (2000). In their paper, CO($J = 2\rightarrow1$) was compared to cold dust continuum at 0.85 mm and 1.2 mm. The 7-$\mu$m emission, however, is emitted from warm dust grains, so it is plausible to find sharp decrease of intensity outside the hot starburst environment. CO($J = 1\rightarrow0$), on the other hand, traces cold gas as well. Although we did not detect CO to the same extent as dust in Kaneda et al. (2010), the NW clump in this work and the CO map in Taylor, Walter, and Yun (2001) indicate that the molecular gas is widely distributed in the halo.

In recent studies the emission from PAHs at 3.3 $\mu$m and aliphatic hydrocarbons at 3.4–3.6 $\mu$m has been detected in the halo of M 82 (Yamagishi et al. 2012). Small particles, such as PAHs, are fragile, and can be destroyed either by ionizing radiation (UV photons from hot stars in the starburst nucleus or the bright X-ray halo of M 82, see Tsuru et al. 2007), or even more effectively by shocks, both likely to occur in galactic winds and starburst environments. Therefore, a problem arises: what is protecting these particles from destruction? Observation points where the 3-$\mu$m features were detected by Yamagishi et al. (2012) are at $\sim 1'.5$ in the north and $\sim 2'$ in the south of the galactic center, which is within the range where CO was detected in our map. From the CO data we suggest that regions with low intensity of CO in the halo far above the galactic plane arise from molecular clouds with an uneven distribution, where the column densities in some places could be high enough to allow self-shielding, and attenuate the penetration of UV photons. Also, if we assume that the clouds are not affected by fast shocks, but entrained in the galactic wind, co-existing with other components, destruction by collisions may be restrained. Sites like the NW clump are likely to be harboring neutral material, such as atomic and molecular gas, PAHs and dust grains. New sensitive observations with higher resolution would better constrain the properties of these neutral gas clouds in the halo.

## 5. Summary

We mapped the CO ($J = 1\rightarrow0$) emission in the archetypal starburst galaxy M 82, including the halo in a large field (15.7 × 16.9 arcmin$^2$) with an angular resolution of 22″, using the NRO 45-m telescope.

1. CO gas was clearly detected in the halo. Most of the emission arises from the molecular clouds within 3 kpc

of the galactic plane. The integrated intensity map shows three main components: the outflow, disk (including the bright nucleus) and streams. The total mass of the molecular gas in the outflow is $(0.26\text{–}1.0) \times 10^9 \, M_\odot$, which is up to $\sim 40\%$ of the total mass of the molecular gas.

2. The position-velocity map along the minor axis of the galaxy indicates CO line splitting in the southern part of the outflow up to $-80''$, and up to $+60''$ in the northern part, including minor components at blueshifted velocities. The molecular gas outflow is predominantly blueshifted in the north, and redshifted in the south, which is expected from a nearly edge-on galaxy with a narrow, cylindrically shaped outflow in addition to a broad diffuse component. The kinetic energy of the molecular gas outflow is estimated to be $(1\text{–}4) \times 10^{56}$ erg.

3. A clump of CO gas was discovered $\sim 3.5$ kpc above the galactic plane. It is coincident with a dark lane in X-ray emission, and a lane of the atomic gas clouds traced with the 21-cm line. The total column density of the neutral gas is on the order of $N_\mathrm{H} \sim 10^{21} \, \mathrm{cm}^{-2}$. The clump is most likely of tidal origin.

4. A comparison with other data, especially with near-IR emission from the molecular hydrogen, dust and PAHs, indicates that the CO gas coexists with these components and may contribute to shielding from intense UV radiation. This would allow the neutral component of the interstellar medium to survive in the halo of M 82. A comparison between CO(1–0) and CO(3–2) clearly shows a lower excitation [CO(3–2)/(1–0) ratio, $R_{31} \simeq 0.5$], of the CO gas in the outflow compared to the central starburst and the galactic disk. The ratio declines from $R_{31} \simeq 1.0$ to $R_{31} \simeq 0.5$ from the nucleus to $|Y| = 40''$ in the halo.

## References

Aalto, S., Garcia-Burillo, S., Muller, S., Winters, J. M., van der Werf, P., Henkel, C., Costagliola, F., & Neri, R. 2012, A&A, 537, A44

Appleton, P. N., Davies, R. D., & Stephenson, R. J. 1981, MNRAS, 195, 327

Chung, A., Yun, M. S., Naraynan, G., Heyer, M., & Erickson, N. R. 2011, ApJ, 732, L15

Chynoweth, K. M., Langston, G. I., Yun, M. S., Lockman, F. J., Rubin, K. H. R., & Scoles, S. A. 2008, AJ, 135, 1983

Cottrell, G. A. 1977, MNRAS, 178, 577

Dame, T. M., Hartman, D., & Thaddeus, P. 2001, ApJ, 547, 792

Draine, B. T. 2011, Physics of the Interstellar and Intergalactic Medium (Princeton: Princeton University Press), 353

de Vaucouleurs, G., de Vaucouleurs, A., Corwin, H. G., Jr., Buta, R. J., Paturel, G., & Fouque, P. 1991, Third Reference Catalogue of Bright Galaxies, Version 3.9 (New York: Springer-Verlag)

Engelbracht, C. W., et al. 2006, ApJ, 642, L127

Fenech, D., Beswick, R., Muxlow, T. W. B., Pedlar, A., & Argo, M. K. 2010, MNRAS, 408, 607

Hoopes, C. G., et al. 2005 ApJ, 619, L99

Hopkins, P. F., Quataert, E., & Murray, N. 2012, MNRAS, 421, 3488

Ichikawa, T., Yanagisawa, K., Itoh, N., Tarusawa, K., van Driel, W., & Ueno, M. 1995, AJ, 109, 2038

Kaneda, H., et al. 2010, A&A, 514, A14

Karachentsev, I. D., et al. 2002, A&A, 383, 125

Lallement, R. 2004, A&A, 422, 391

Lehnert, M. D., Heckman, T. M., & Weaver, K. A. 1999, ApJ, 523, 575

Lo, K. Y., Cheung, K. W., Masson, C. R., Phillips, T. G., Scott, S. L., & Woody, D. P. 1987, ApJ, 312, 574

Lynds, C. R., & Sandage, A. R. 1963, AJ, 137, 1005

Mangum, J. G., Emerson, D. T., & Greisen, E. W. 2007, A&A, 474, 679

Martin, C. L. 1998, ApJ, 506, 222

Mayya, Y. D., Bressan, A., Carrasco, L., & Hernandez-Martinez, L. 2006, ApJ, 649, 172

Mayya, Y. D., Carrasco, L., & Luna, A. 2005, ApJ, 628, L33

Miller, J. M., Nowak, M., Markoff, S., Rupen, M. P., & Maitra, D. 2010, ApJ, 720, 1033

Murray, N., Quataert, E., & Thompson, T. A. 2005, ApJ, 618, 569

Nakai, N., Hayashi, M., Handa, T., Sofue, Y., Hasegawa, T., & Sasaki, M. 1987, PASJ, 39, 685

Nakai, N., & Kuno, N. 1995, PASJ, 47, 761

Nakanishi, H., & Sofue, Y. 2006, PASJ, 58, 847

Narayanan, D., et al. 2008, ApJS, 176, 331

Narayanan, D., Krumholz, M. R., Ostriker, E. C., & Hernquist, L. 2012, MNRAS, 421, 3127

Nieten, Ch., Neininger, N., Guélin, M., Ungerechts, H., Lucas, R., Berkhuijsen, E. M., Beck, R., & Wielebinski, R. 2006, A&A, 453, 459

Nilson, P. 1973, Uppsala Astron. Obs. Ann., 6

O'Connell, R. W., Gallagher, J. S., III., Hunter, D. A., & Colley, W. N. 1995, ApJ, 446, L1

Ohyama, Y., et al. 2002, PASJ, 54, 891

Oloffson, H., & Rydbeck, G. 1984, A&A, 136, 17

Rieke, G., Lebofsky, M., Thompson, R., Low, F., & Tokunaga, A. 1980, ApJ, 238, 24

Roussel, H., et al. 2010, A&A, 518, L66

Sandage, A., & Brucato, R. 1979, AJ, 84, 472

Sawada, T., et al. 2008, PASJ, 60, 445

Seaquist, E. R., & Clark, J. 2001, ApJ, 552, 133

Shen, J., & Lo, K. Y. 1995, ApJ, 445, L99

Shopbell, P. L., & Bland-Hawthorn, J. 1998, ApJ, 493, 129

Snow, T. P., & McCall, B. J. 2006, ARA&A, 44, 367

Sofue, Y. 1998, PASJ, 50, 227

Sorai, K., Sunada, K., Okumura, S. K., Iwasa, T., Tanaka, A., Natori, K., & Onuki, H. 2000, Proc. SPIE, 4015, 86

Stevens, I. R., Read, A. M., & Bravo-Guerrero, J. 2003, MNRAS, 343, L47

Strickland, D. K., Heckman, T. M., Colbert, E. J. M., Hoopes, C. G., & Weaver, K. A. 2004, ApJ, 606, 829

Sunada, K., Yamaguchi, C., Nakai, N., Sorai, K., Okumura, S. K., & Ukita, N. 2000, Proc. SPIE, 4015, 237

Taylor, C. L., Walter, F., & Yun, M. S. 2001, ApJ, 562, L43

Tenorio-Tagle, G., & Bodenheimer, P. 1988, ARA&A, 26, 145

Thuma, G., Neininger, N., Klein, U., & Wielebinski, R. 2000, A&A, 358, 65

Tsuru, T. G., et al. 2007, PASJ, 59, S269

Tsuru, T. G., Awaki, H., Koyama, K., & Ptak, A. 1997, PASJ, 49, 619

Tully, R. B. 1988, Science, 242, 310

Ulich, B. L., & Haas, R. W. 1976, ApJ, 30, 247

van Dishoeck, E. F., & Black, J. H. 1988, ApJ, 334, 771

Veilleux, S., Cecil, G., & Bland-Hawthorn, J. 2005, ARA&A, 43, 769

Veilleux, S., Rupke, D. S. N., & Swaters, R. 2009, ApJ, 700, L149

Walter, F., Weiss, A., & Scoville, N. 2002, ApJ, 580, L21

Weiß, A., Neininger, N., Hüttemeister, S., & Klein, U. 2001, A&A, 365, 571

Weiß, A., Walter, F., & Scoville, N. Z. 2005, A&A, 438, 533

Yamagishi, M., Kaneda, H., Ishihara, D., Kondo, T., Onaka, T., Suzuki, T., & Minh, Y. C. 2012, A&A, 541, A10

Yoshida, M., Kawabata, K. S., & Ohyama, Y. 2011, PASJ, 63, S493

Young, J. S., & Scoville, N. Z. 1991, ARA&A, 29, 581

Yun, M. S., Ho, P. T. P., & Lo, K. Y. 1993, ApJ, 411, L17

Yun, M. S., Ho, P. T. P., & Lo, K. Y. 1994, Nature, 372, 530